PAPER

Strong plasmon–exciton coupling between lithographically defined single metal nanoparticles and monolayer WSe$_2$†

Xiaohong Yan [ID] [a,b] and Hong Wei [ID] *[a,c]

Strong coupling between surface plasmons and excitons leads to the formation of plexcitons with new energy states, providing a versatile platform for a range of frontier research subjects. Single plasmonic nanoparticles have recently attracted much attention for realizing strong coupling due to their small mode volume. However, the usually used chemically synthesized metal nanoparticles are unfavorable for accurately tailoring the surface plasmon resonances and adverse to the implementation of on-chip integration. Here, we report for the first time the realization of strong coupling between monolayer WSe$_2$ and lithographically defined single metal nanoparticles. Focusing on gold nanobowties, the large Rabi splitting of 187 meV is achieved. The excitons around the nanogaps in the nanobowties contribute dominantly to the coupling strength, and the coupling strength is larger for smaller nanobowties due to the smaller mode volume. Moreover, the hybrid systems of monolayer WSe$_2$ and gold nanoparticle monomers of nanorods, nanotriangles, and nanodisks are found to closely satisfy the criterion of strong coupling. The strong plasmon–exciton coupling realized by single plasmonic nanostructures fabricated by advanced nanofabrication techniques and monolayer semiconductors can provide new opportunities for manipulating strong light–matter interactions at the nanoscale and facilitate the development of plexciton-based nanodevices with ultrasmall footprints.

Introduction

Cavity quantum electrodynamics has long been a central subfield of quantum optics for the study of cavity-involved light–matter interactions. The optical cavity has the ability to manipulate the local electromagnetic environment around the quantum emitter, and thus alters its decay rate, which can be understood by Fermi's golden rule. When the light–matter interactions are strong enough to reach the strong coupling regime, exciton polaritons with new energy states are produced, which in plasmonic hybrid systems are usually called plasmon–exciton polaritons or plexcitons. The exciton polariton inherits both the properties of light and matter, and can serve as a promising platform for the Bose–Einstein condensation (BEC),[1–4] the suppression of the photo-oxidation of

organic chromophores,[5] coherent emission or absorption,[6,7] topological insulators,[8–10] lasing,[11,12] and so on.

To realize the strong coupling, the Rabi splitting should be larger than the mean linewidth of the uncoupled systems.[13,14] Given the coupling strength is the scalar product of the emitter's transition dipole moment and the vacuum electric field, the cavity with smaller mode volume, which leads to stronger vacuum electric field, and the quantum emitter with larger transition dipole moment, are preferred. Metal nanostructures, especially coupled nanostructures, can confine electromagnetic field into tiny spaces of deep subwavelength scale due to the excitation of surface plasmons (SPs),[15,16] resulting in a very small mode volume. Therefore, plasmonic nanocavities are favorable for realizing strong coupling at the nanometer scale. Using single metal nanoparticles supporting localized SPs, strong coupling has been realized at the single exciton level for molecules[17,18] and quantum dots,[19–22] and at a small number of excitons level for the monolayers of transition metal dichalcogenides (TMDs).[23–27] The monolayers of TMDs possess direct bandgaps, large transition dipole moments, and small linewidths,[14,28] and thus are promising platforms for studying the strong coupling phenomena. Besides, the exotic features of the monolayer TMDs, such as the locked spin and valley degrees of freedom,[29] chemical inertness, atomic thickness,

[a]*Beijing National Laboratory for Condensed Matter Physics, Institute of Physics, Chinese Academy of Sciences, Beijing 100190, China. E-mail: weihong@iphy.ac.cn*
[b]*School of Physical Sciences, University of Chinese Academy of Sciences, Beijing 100049, China*
[c]*Songshan Lake Materials Laboratory, Dongguan 523808, China*
†Electronic supplementary information (ESI) available. See DOI: 10.1039/d0nr01056a

and the flexibility for integration,[30,31] extend their applications. In recent years, strong coupling between monolayer TMDs and cavity modes has been reported for the photonic modes in cavities formed by distributed Bragg reflectors[32–34] or metal mirrors,[35,36] the surface lattice resonance modes in the arrays of metal nanoparticles or nanoholes in metal films,[36–39] the localized SP modes supported by metal nanoparticles,[23–27] and both the nanoparticle SP and optical cavity modes formed by metal mirrors.[40,41] In the study of strong coupling between single metal nanoparticles and TMD monolayers, chemically synthesized metal nanoparticles were usually used. To our knowledge, strong coupling between lithographically defined single metal nanoparticles and monolayer TMDs is lacking. Since the lithographically defined metal nanostructures are highly compatible with on-chip integration, their strong coupling with TMDs will largely benefit the development of plexciton-based nanophotonic devices.

Here, we investigate the strong coupling between lithographically defined isolated Au nanostructures and monolayer WSe$_2$. Focusing on Au nanobowties, we tune the SP resonance peak across the exciton energy of the monolayer by varying the size of nanoparticles and collecting the scattering light with different polarizations. The large Rabi splitting of 187 meV, exceeding the mean linewidth of SPs and excitons, proves the realization of strong coupling. For Au nanoparticle monomers, including nanodisks, nanotriangles and nanorods, the Rabi splitting is close to the strong coupling conditions. Coupled oscillator model and numerical simulations are applied to analyze the strong coupling, agreeing well with the experimental results.

Methods

Fabrication of gold nanostructures

Gold nanostructures of 30 nm thickness were fabricated on a SiO$_2$/Si substrate with a SiO$_2$ layer of 90 nm by electron beam lithography (EBL) and electron beam evaporation of Au films. Polymethylmethacrylate (PMMA) (950K A2) resist was spin-coated on top of the substrate at the speed of 4000 rpm, followed by baking on a hot plate (180 °C, 1 min) to obtain a uniform film of ~80 nm thick. The electron beam exposure on the PMMA resist was performed using a Raith 150 EBL system (accelerating voltage 20 kV, aperture 7.5 μm and beam current 18.5 pA). The adjacent nanostructures were separated by 2 μm. After the exposure, the sample was washed in the cold (~5 °C) developer (methyl isobutyl ketone (MIBK) : isopropyl alcohol (IPA) = 1 : 3) for 40 s, followed by immersion in the fixer (IPA) for 30 s. Gold films of 30 nm thickness were deposited using an electron beam evaporator (Peva-600E) at a speed of 1 Å s^{-1}. To decrease the loss of plasmonic nanostructures, we abandoned the standard deposition method with the adhesion layer,[42] and employed a dry lift-off method.[43] The dry lift-off process was performed as follows. First, a small piece of transparent adhesive tape was stuck at the edge of the gold layer.

Second, polyvinyl alcohol (PVA) water solution (5 wt%) was dropped on both the gold layer and the tape, and baked at 60 °C on a hot plate for 30 min. Third, the PVA layer with gold not contacting the substrate was lifted off by removing the tape. Finally, the PMMA layer was removed by reactive-ion etching (RIE) (PlasmaPro NGP80), with oxygen cleaning (flow rate 50 sccm, pressure 100 mTorr, power 100 W and DC bias 271 V) for 10 cycles (etching 1 min and cooling 30 s for one cycle).

Optical measurements

An upright microscope (BX51, Olympus) with a bright-field/dark-field objective (100×, NA 0.90) was used to collect both the bright- and dark-field images of the sample, and the dark-field scattering spectra of the isolated gold nanostructures were recorded using a spectrograph (Princeton Instruments, Acton SP2500). A rotatable polarizer (U-AN360P, Olympus) was installed in the collection path to record the spectra with different polarizations.

Numerical simulations

Simulations were performed by the finite element method (FEM) (COMSOL Multiphysics). In our simulation, a two-step calculation was employed.[27] In both of the two steps, we solved for the scattered field. In the first step, a plane wave polarized along the long axis of Au nanobowties at normal incidence was set as the background electric field. The full electric field (the sum of the background electric field and the scattered field) in the absence of the Au nanobowties obtained in the first step was adopted as the background electric field for the scattered field simulation in the second step. The far field was obtained by the near-to-far field transformation based on the Stratton-Chu formula, and the simulated scattering spectra were obtained by the integration of the far field within the solid angle of 2arcsin(NA), with NA = 0.9 to mimic our experimental conditions.[44]

The scattered electric field of the second step calculation was regarded as the near field of the SP mode, and the simulated time-averaged energy density is given by

$$W(\mathbf{r}) = \frac{1}{4}\left(\frac{\partial[\omega\varepsilon'(\mathbf{r})]}{\partial\omega}\varepsilon_0|\mathbf{E}(\mathbf{r})|^2 + \mu_0|\mathbf{H}(\mathbf{r})|^2\right), \quad (1)$$

where $\mathbf{E}(\mathbf{r})$, $\mathbf{H}(\mathbf{r})$ and $\varepsilon'(\mathbf{r})$ denote the electric field, the magnetic field and the real component of permittivity at position $\mathbf{r}$, ε_0 and μ_0 are the permittivity and permeability of the vacuum, and ω is the angular frequency of the electric field.

The mode volume of the SP mode is calculated by normalizing the integration of the energy density to its maximum:

$$V = \frac{\int W(\mathbf{r})d^3\mathbf{r}}{\max[W(\mathbf{r})]}, \quad (2)$$

where the integration domain was truncated by eliminating the influence of the radiative loss with linear divergence.[45]

Assuming the total energy distribution of the vacuum field mimics its counterpart of the simulated SP mode, the vacuum electric field can be obtained as

$$|\mathbf{E}_{\text{vac}}(\mathbf{r})| = |\mathbf{E}(\mathbf{r})| \sqrt{\frac{\frac{1}{2}\hbar\omega}{\int W(\mathbf{r})\mathrm{d}^3\mathbf{r}}}. \tag{3}$$

Results and discussion

After obtaining the Au nanostructures, WSe$_2$ monolayers on the sapphire substrate grown by a chemical vapor deposition method were transferred to accurate positions on top of the Au nanostructures using a home-made transfer station (see section 1 in the ESI†) to obtain the coupled system, as schematically shown in Fig. 1a. By measuring the same Au nanostructures before and after transferring the monolayer WSe$_2$, we can reveal how the monolayers influence the SP resonance wavelengths and the scattering spectra of the plasmonic nanostructures. Fig. 1b shows the dark-field optical image of Au nanobowties of different sizes covered by WSe$_2$ monolayers, where the bright white dots and curves indicate the nanobowties and the WSe$_2$ layer boundaries, respectively. The top inset shows the bright-field image of the area outlined by the white dashed rectangle, where the nanobowties and monolayer WSe$_2$

can be identified as the periodic black dots and large light black areas. The uniform optical contrast of the light black areas in the bright-field image (see also Fig. S2 in the ESI†) indicates the uniformity of the monolayer WSe$_2$. The monolayer nature of WSe$_2$ was confirmed by Raman measurements (see section 3 in the ESI†). The exciton energy can obtained from the transmission spectra (see section 4 in the ESI†). We focus on the A exciton with the photoluminescence (PL) peak at ∼750 nm (top spectrum in Fig. 1c and see also Fig. S8 in the ESI†).

The SP resonance wavelength can be tuned by the nanoparticle size to overlap with the exciton energy. For the coupled system of a Au nanobowtie and monolayer WSe$_2$, the peak in the dark-field scattering spectrum splits, as can be seen in the green spectrum in Fig. 1c. We also fabricated monomers of nanotriangles, nanodisks, and nanorods, and peak splitting was also observed for these nanoparticles coupled with WSe$_2$ monolayers, as shown by the three spectra at the bottom in Fig. 1c.

We measured the dark-field scattering spectra of Au nanobowties of different sizes before and after transferring the monolayer WSe$_2$. After the spectroscopy measurements, the SEM images of the corresponding nanostructures were acquired. The nanobowtie has two dipolar SP modes, i.e., longitudinal and transverse SP modes, which can be excited by the light polarized parallel and perpendicular to the long axis
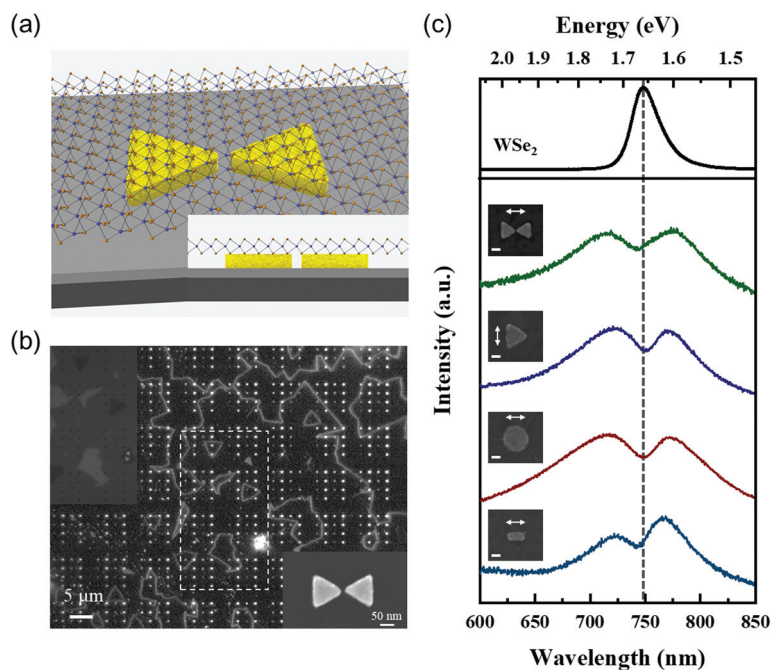

Fig. 1 (a) Schematic of the hybrid structure of a Au nanobowtie and the monolayer WSe$_2$. The nanobowtie is on a SiO$_2$/Si substrate. The inset shows the front view of the structure. (b) The dark-field optical micrograph of the Au nanobowties and the WSe$_2$ layer. The bright white dots and curves denote the nanobowties and the WSe$_2$ boundaries, respectively. The top inset is the bright-field optical micrograph of the area in the white dashed box, where the arrayed black dots indicate the nanobowties, the large light black areas indicate the monolayer WSe$_2$, and the dark black or bright triangles are the multilayer WSe$_2$. The bottom inset shows a scanning electron microscopy (SEM) image of a Au nanobowtie before WSe$_2$ transfer. (c) The PL spectrum of the monolayer WSe$_2$ (top) and the normalized scattering spectra of various Au nanostructures coupled with monolayer WSe$_2$ (bottom). Insets show the SEM images of the corresponding coupled nanostructures, and the white arrows indicate the polarization directions. The scale bars are 50 nm.

of the bowtie, respectively.[19,46–48] The two modes were observed by measuring the spectra of scattering light polarized parallel or perpendicular to the long axes of the nanobowties. Here, we kept the nanogaps of the bowties to be around 10 nm, and varied the side lengths to tune the SP resonance peaks across the exciton energy. Larger side lengths lead to longer resonance wavelengths, as shown by the scattering spectra in blue in Fig. 2a and c for the nanobowties shown in Fig. 2b. The smaller nanogaps in the nanobowties lead to smaller mode volume, and thus benefit the realization of strong coupling.[49] Therefore, we fabricated the nanobowties with gaps as small as possible, which are among the best structures based on lithography technologies.[19,47]

After the transfer of WSe₂ monolayers, two peaks were observed in the scattering spectra (red lines in Fig. 2a and c). The intensity ratio of the longer wavelength peak (lower branch (LB)) and shorter wavelength peak (upper branch (UB)) increases with the increase of the nanotriangle size. Since the resonance wavelength of the longitudinal mode is longer than that of the transverse mode, the peak wavelength in the scattering spectra can be tuned by the polarization of the scattering light due to the variation of the proportions of these two modes. For a Au nanobowtie coupled with a WSe₂ monolayer,

by changing the polarization angle of the analyzer in the detection light path, the relative intensity of the two peaks gradually varied (Fig. 2d), similar to the results in Fig. 2a and c. The longer resonance wavelength of the longitudinal mode indicates that smaller nanobowties can be selected for the plasmon–exciton strong coupling, which help to decrease the loss and mode volume. Therefore, we focused on the coupling of the longitudinal SP mode with the excitons of WSe₂ monolayers.

To analyze the experimental results of plasmon–exciton interactions, we make use of the coupled oscillator model (see section 6 in the ESI†). As a result of extremely small linewidths of the SPs and excitons compared with their resonance energies, the energies of the plexciton states can be written as

$$E_{\pm} = \frac{E_{SP} + E_X}{2} \pm \sqrt{g^2 + \frac{\delta^2}{4}}, \qquad (4)$$

where E_{SP} and E_X are the resonance energies of the SPs and excitons, respectively, g is the coupling strength between them, and $\delta = E_{SP} - E_X$ is the detuning of the SP mode relative to the exciton state. From each of the scattering spectra of the nanobowtie-WSe₂ hybrid structures, we can extract the peak ener-
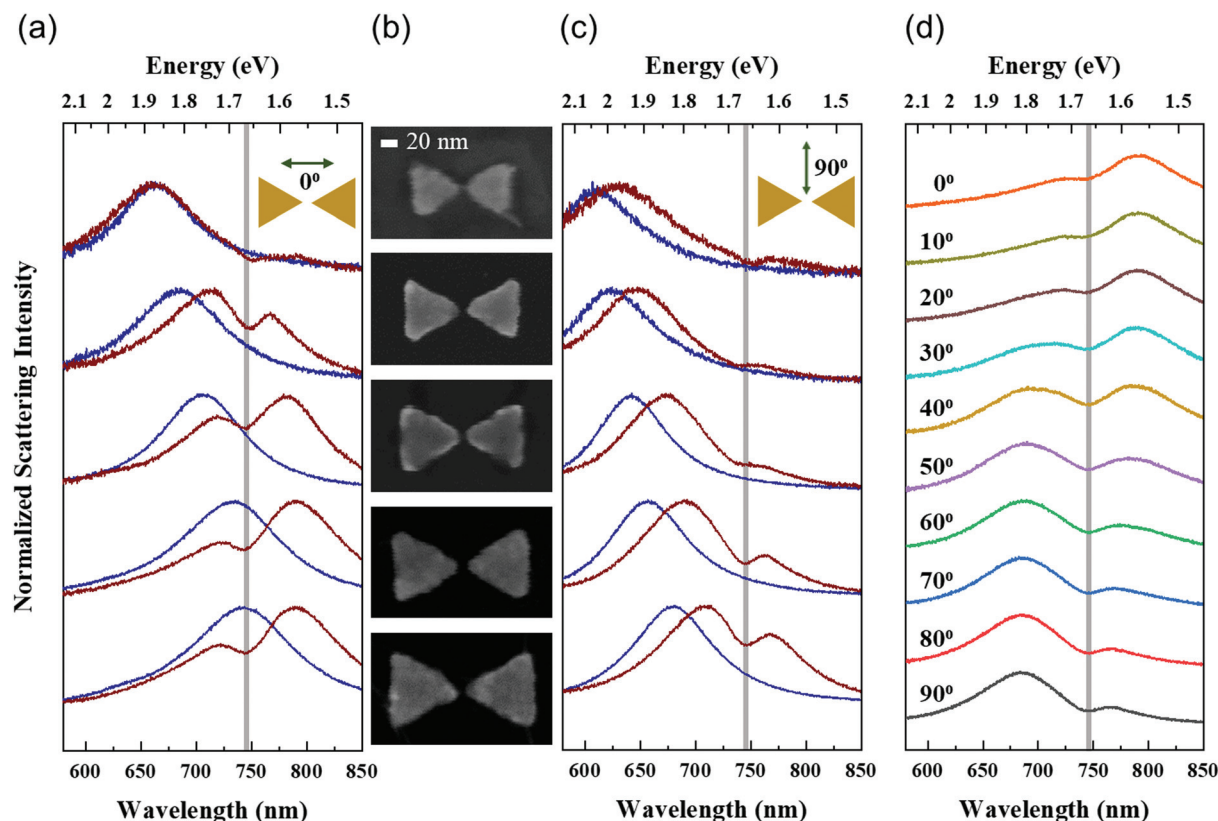

Fig. 2 (a and c) The scattering spectra for the longitudinal (a) and transverse (c) modes of single Au nanobowties with different sizes before (blue lines) and after (red lines) monolayer WSe₂ transfer. The green arrows indicate the polarization directions of the scattering light. (b) The corresponding SEM images of the Au nanobowties after the WSe₂ transfer. The side length of the nanotriangle is set as 70, 80, 90, 100, and 110 nm, respectively, and the actual lengths are close to the set values. (d) The scattering spectra of a nanobowtie coupled with monolayer WSe₂ for different detection polarizations. The definition of the polarization angles is consistent with that shown in (a) and (c).

gies of both UB (E_+) and LB (E_-). Therefore, the SP resonance energy can be obtained as $E_{SP} = E_+ + E_- - E_X$. It is noted that the SP resonance energy obtained in this way is different from the one obtained from the scattering spectrum before the monolayer WSe$_2$ transfer, which results from the dielectric environment variation caused by the monolayer with high refractive index and will be analyzed later.

The red circles in Fig. 3a show the eigenenergies of UB and LB for the longitudinal mode as a function of the detuning, corresponding to nanobowties with similar nanogaps (~10 nm) and varied side lengths. By fitting the scatter diagram with eqn (4) (solid black lines in Fig. 3a), we achieve the large Rabi splitting of 187 meV at zero detuning, which is larger than the mean linewidth of the SPs (204 meV) and excitons (55 meV), i.e., 130 meV, confirming the achievement of strong coupling. In this fitting, the coupling strength is assumed as a constant value for all nanobowties. However, actually, different Au nanobowties may lead to different coupling strengths, which results in the clear deviation of some experimental data points from the fitting lines and will be analyzed later. The orange shadows in Fig. 3a show the range of the UB and LB for different coupling strengths with the inner and outer boundaries corresponding to the minimal and maximal coupling strengths, respectively.

Based on the fitting results, the fractions of SPs and excitons both in the UB and LB can be derived (Fig. 3b and c, and see section 6 in the ESI†). The fractions of the SPs and excitons are equal at zero detuning for both plexciton branches, indicating the identical weight of SPs and excitons in the mixed states. For the UB, the fraction of SPs is larger than that for excitons for the positive detuning, but the fraction of excitons dominates for the negative detuning. The variation of SP and exciton weights as a function of detuning in Fig. 3b is consistent with the asymptotic results of the UB in Fig. 3a. The fitting results in Fig. 3a show that the UB energy gets close to the SP energy as the positive detuning increases, while it gets close to the exciton energy as the negative detuning increases. For the LB, the fraction of SPs (excitons) coincides with the fraction of excitons (SPs) in the UB, matching the theoretical predictions.[50]

Besides Au nanobowties, similar measurements and analyses were performed for the monomers of Au nanodisks, nanotriangles and nanorods coupling with WSe$_2$ monolayers (see section 7 in the ESI†). Fig. 3d shows the Rabi splitting as a function of mean linewidth of the SPs and excitons for the three nanoparticle monomers and nanobowties. The black solid line $\hbar\Omega = (\Gamma_{SP} + \Gamma_X)/2$ separates the entire domain into two distinct areas: the strong coupling regime and the weak coupling regime. The nanobowties strictly satisfy the criterion of strong coupling with the Rabi splitting larger than that of the nanotriangle and nanorod monomers. Although all of these three monomers do not strictly satisfy the criterion of strong coupling, they are all close to meeting it. For the same resonance wavelength, the longitudinal SP mode of the nano-
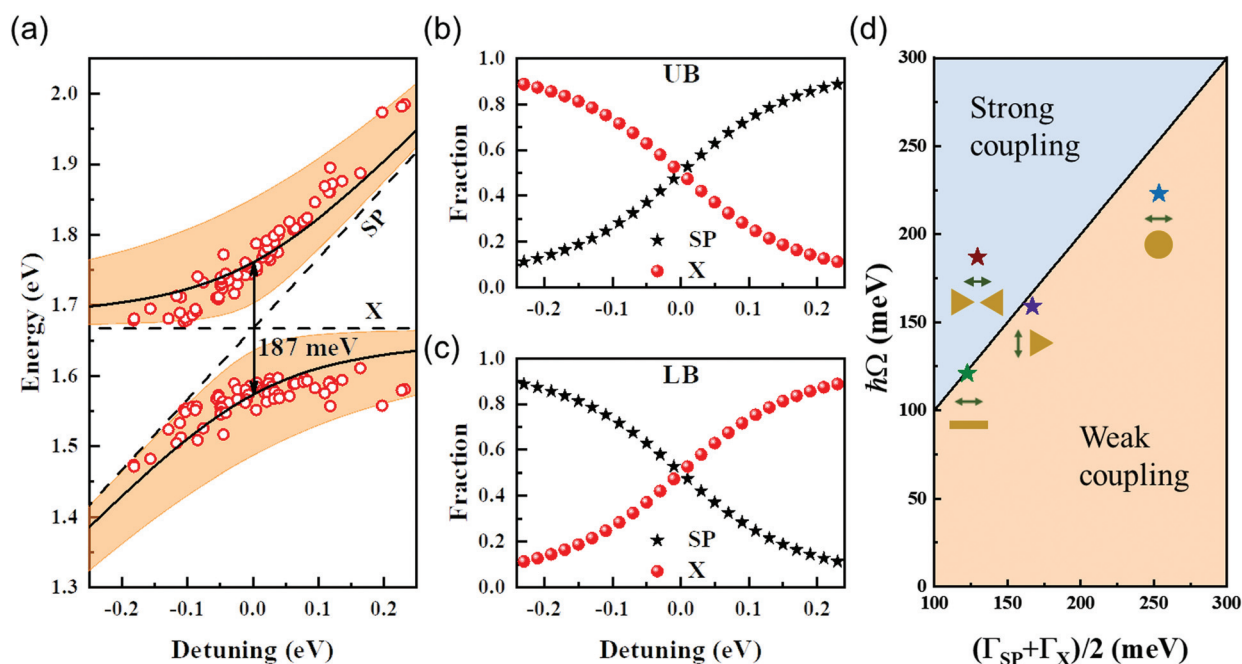

Fig. 3 (a) The extracted peak energies (red circles) of the scattering spectra as a function of detuning for Au nanobowties coupled with monolayer WSe$_2$. The black solid lines are the fitting results with the coupling strength of 93.5 meV, and the black dashed lines indicate the energies of the uncoupled SPs and excitons (X). The orange areas are between the boundary curves representing the plexciton energies for the minimal (33.2 meV) and maximal (183.0 meV) coupling strengths. (b and c) The fractions of SPs (black stars) and excitons (red balls) in the upper (b) and lower (c) branches of the plexciton states. (d) Comparison of the Rabi splitting and the mean linewidth of the coupled systems of monolayer WSe$_2$ and different kinds of Au nanostructures.

bowties has a smaller linewidth in comparison with the nano-triangles. Among the three monomers with the same reso-nance wavelength, the linewidth of the nanorod is minimum. This is because, in dipolar approximation, the radiative decay rate, which dominantly determines the linewidth of the scat-tering spectrum in our experiment, is proportional to the nanoparticle volume,[51,52] and the nanorod has the smallest volume among the three monomers.

To further understand the strong coupling, we performed FEM simulations. The permittivity of Au and Si are taken from the literature.[53,54] The refractive index of air and SiO$_2$ are set as 1 and 1.5, respectively. The in-plane permittivity of monolayer WSe$_2$ is obtained based on our transmission measurements (see section 4 and Fig. S6 in the ESI†) and the literature,[55] and can be described by the Lorentz model:

$$\varepsilon_{in} = \varepsilon_\infty + f_A \frac{\omega_A{}^2}{\omega_A{}^2 - \omega^2 - i\gamma_A\omega} + f_B \frac{\omega_B{}^2}{\omega_B{}^2 - \omega^2 - i\gamma_B\omega}, \quad (5)$$

where $\varepsilon_\infty = 15.5$ is the background permittivity corresponding to higher energy transitions, and $\omega_A(\omega_B)$, $\gamma_A(\gamma_B)$, and $f_A(f_B)$ are the exciton transition frequency, linewidth, and the reduced oscillator strength of A (B) exciton, respectively. Since the ω_B

= 2.119 eV (i.e., 585.1 nm) is beyond the wavelength range of our interest, we combined the contribution of B exciton and ε_∞ as the final background permittivity. The out-of-plane per-mittivity of the monolayer WSe$_2$ is set as 2.9.[23,56,57] The thick-nesses of SiO$_2$ and monolayer WSe$_2$ are set as 90 nm and 0.7 nm, respectively, coinciding with our experimental parameters.

Due to the high refractive index of the monolayer WSe$_2$, coating the metal nanostructures with the monolayer WSe$_2$ can induce the redshift of the SP resonance, just like the red-shift caused by other dielectric coating layers.[23] To demon-strate the influence of the high refractive index of the mono-layer, we simulated the scattering spectra for the Au nanobow-ties before and after being coated with a dielectric layer (blue solid and dashed lines in Fig. 4a). The in-plane permittivity of the dielectric layer is obtained from eqn (5) by setting $f_A = 0$ (Fig. S7 in the ESI†). After adding the dielectric layer, the peak of the calculated scattering spectrum is red-shifted and located between the two peaks of the scattering spectrum of a Au nanobowtie strongly coupling with the monolayer WSe$_2$ (Fig. 4a, red solid lines). The calculated spectral redshift is about 30–50 nm, comparable with the values extracted from the experimental results (Fig. S10 in the ESI†). The simulated
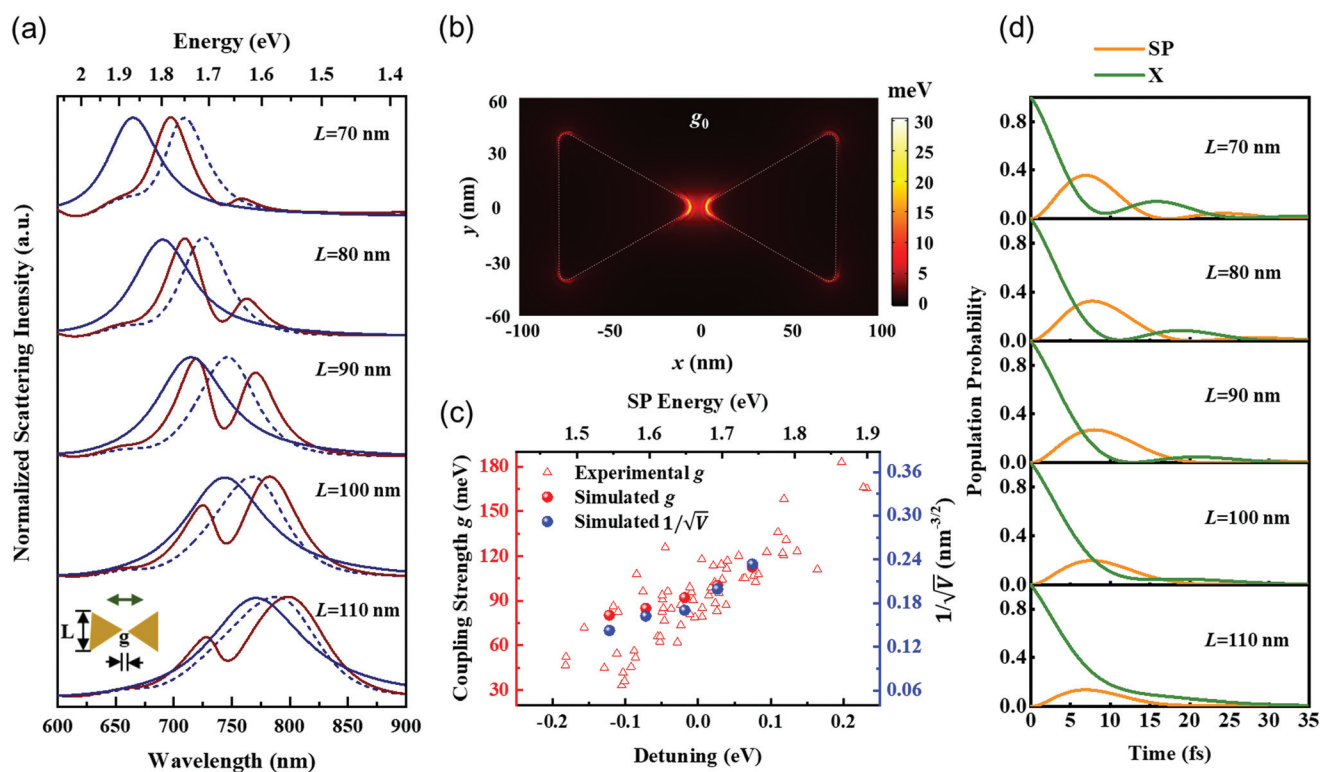

Fig. 4 (a) Simulated far-field scattering spectra for the structures of bare Au nanobowtie (blue solid lines), nanobowtie covered by a dielectric layer (blue dashed lines), and nanobowtie covered by the monolayer WSe$_2$ (red solid lines) for polarization along the long axis of the bowtie. The gap size is maintained at 10 nm. The side length L is increased from 70 to 110 nm. (b) Simulated distribution of the single exciton coupling strength for a Au nanobowtie (with the side length of 90 nm and gap size of 10 nm) with the monolayer WSe$_2$ on top. (c) The experimental (red triangles) and simu-lated (red balls) coupling strength g and simulated $1/\sqrt{V}$ (blue balls) as a function of detuning for strong coupling between the longitudinal SP mode of the Au nanobowties and the exciton state of the monolayer WSe$_2$. (d) The calculated transient dynamics of the population probabilities for the SPs and excitons based on the FEM simulation results in (a) and (c).

results of bare nanobowties and nanobowties covered by monolayer WSe$_2$ agree well with the experimental results in Fig. 2a, proving the credibility of our measurements.

Theoretically, the coupling strength of a single exciton and a cavity mode is defined as $g_0 = \mathbf{\mu} \cdot \mathbf{E}_{vac}$, and the magnitude of the vacuum electric field is $|\mathbf{E}_{vac}| = \sqrt{\hbar\omega/2\varepsilon V}$, where ε is the permittivity of the material inside the cavity. For the cavity mode with uniform electric field, the mode volume V determines the magnitude of the vacuum field, and thus the coupling strength. However, around a metal nanoparticle, the electric field has a large gradient due to the field confinement of the SP mode. Therefore, the quantum emitters sense different electric fields at different positions. The coupling strength of an emitter located at different positions around the nanoparticle gives further information beyond the mode volume. To plot the distribution of the single exciton coupling strength, we should figure out both the transition dipole moment of the exciton in the monolayer WSe$_2$ and the vacuum electric field surrounding the exciton. Based on the transmission measurements, the transition dipole moment of 7.835 D is obtained (see section 9 in the ESI†), which is similar to the result of 7.675 D extracted from the literature.[23] The vacuum electric field can be obtained from the FEM simulation. Fig. 4b shows the distribution of single exciton coupling strength at the bottom surface of the monolayer on top of a Au nanobowtie with the side length of 90 nm and gap size of 10 nm. The maximum coupling strength of over 30 meV is obtained at the position just above the bowtie tips. Due to the same transition dipole moment in the monolayer plane, the single exciton coupling strength shares the same distribution as the in-plane electric field.

To obtain the total coupling strength between the Au nanobowtie and the monolayer WSe$_2$, we sum the contributions from all of the excitons, that is, $g = \sqrt{\sum_i g_0{}^2(\mathbf{r}_i)}$, with $g_0(\mathbf{r}_i)$ denoting the coupling strength for a single exciton at the position $\mathbf{r}_i$. Given that the exciton of the monolayer WSe$_2$ has a radius r_0 of 1 nm, we make use of the integration form $g = \sqrt{\dfrac{\int g_0{}^2(\mathbf{r})\mathrm{d}S}{\pi r_0{}^2}}$ to obtain the coupling strength between the Au nanobowtie and the monolayer WSe$_2$.[57] The calculation results show that the nanobowties with smaller side lengths lead to larger coupling strengths (Fig. 4c, red balls), which follows the trend of $1/\sqrt{V}$ (Fig. 4c, blue balls). Given the coupling strength $g \propto \sqrt{\dfrac{N}{V}}$, where N is the number of excitons coupling with the SP mode, the coupling strength should also depend on N. However, the excitons around the nanogap dominate the contributions of the coupling strength. For example, for a nanobowtie with 90 nm side length and 10 nm gap distance, the excitons within a circular area with the radius of 20 nm and the center above the center of the nanogap contributes 80.4% of the coupling strength. Therefore, we can neglect the variation of N for nanobowties of different sizes. According to the

formula $g = \sqrt{(\omega_+ - \omega_X)(\omega_X - \omega_-)}$ (see section 6 in the ESI†), the experimental coupling strength can be derived (Fig. 4c, red triangles), which fits well with the simulated results. Looking back at Fig. 3a, it can be seen that there is a slight difference between the experimental results and the black solid fitting lines. This is because the fitting lines are results obtained with an "averaged" coupling strength for all nanostructures. In Fig. 3a, the energies of the two branches extracted from the scattering spectra are between the fitting lines for the negative detuning, but are beyond the fitting lines for the positive detuning, due to the smaller and larger coupling strengths for the negative and positive detuning, respectively. Fig. 4c also shows that the Rabi splitting is decreased for larger nanobowties. Although the SP linewidth is increased with the increase of the nanobowtie size, resulting in reduced energy difference between the Rabi splitting and the mean linewidth of SPs and excitons for larger nanobowties, the strong coupling conditions still hold true (see section 10 in the ESI†).

We also calculated the temporal response of the coupled systems. The Hamiltonian model was adopted to obtain the transient dynamics of the population probabilities for the SPs and excitons (Fig. 4d) based on our FEM simulation results, with the exciton mode initially excited.[58] The ultrafast energy transfer between the SPs and excitons, as well as the rapid decay of the total energy in the coupled system, can be observed from the time-dependent population probabilities and their envelopes in Fig. 4d. The Rabi oscillation is clearly seen for smaller nanobowties. For large nanobowties, as a result of their large decay rates, both the population probabilities of the SPs and excitons decay quickly to approach zero, different from the Rabi oscillation behavior for the smaller ones. The Rabi oscillation period is about 22 fs for the nanobowtie with the side length of 90 nm and gap size of 10 nm whose SP resonance energy is near the zero detuning, similar to the result obtained from the experimental value of Rabi splitting using the relation $T_R \approx \dfrac{2\pi}{\Omega}$, where T_R and Ω represent the Rabi oscillation period and the Rabi splitting frequency, respectively.

Conclusion

We have realized strong plasmon–exciton coupling between lithographically defined single metal nanoparticles and monolayer WSe$_2$. The SP resonance energy can be easily tuned by altering the nanoparticle size and collecting the scattering light with different polarization angles. Among the four kinds of Au nanostructures, the nanobowties strictly satisfy the criterion of strong coupling, and the other three monomers are close to meeting the criterion. For the hybrid systems of single Au nanobowties and monolayer WSe$_2$, both the experimental and simulation results show that larger coupling strength occurs for smaller nanoparticles. In addition, the *in situ* measurements of the same Au nanobowties before and after transferring the monolayer WSe$_2$ help to reveal the large red-

shift of the SP resonance wavelength induced by the high permittivity of the monolayer. Due to the easy implementation of plexciton states, tunability of SP resonances and compatibility with on-chip integration, the hybrid systems we investigated are able to serve as a promising platform for both the fundamental research of strong light–matter interactions at the nanoscale and nanophotonic device applications.

Conflicts of interest

There are no conflicts to declare.

Acknowledgements

References

1 H. Deng, G. Weihs, C. Santori, J. Bloch and Y. Yamamoto, *Science*, 2002, **298**, 199–202.

2 J. Kasprzak, M. Richard, S. Kundermann, A. Baas, P. Jeambrun, J. M. J. Keeling, F. M. Marchetti, M. H. Szymańska, R. André, J. L. Staehli, V. Savona, P. B. Littlewood, B. Deveaud and L. S. Dang, *Nature*, 2006, **443**, 409–414.

3 J. D. Plumhof, T. Stöferle, L. Mai, U. Scherf and R. F. Mahrt, *Nat. Mater.*, 2013, **13**, 247.

4 G. Lerario, A. Fieramosca, F. Barachati, D. Ballarini, K. S. Daskalakis, L. Dominici, M. De Giorgi, S. A. Maier, G. Gigli, S. Kéna-Cohen and D. Sanvitto, *Nat. Phys.*, 2017, **13**, 837.

5 B. Munkhbat, M. Wersäll, D. G. Baranov, T. J. Antosiewicz and T. Shegai, *Sci. Adv.*, 2018, **4**, eaas9552.

6 S. Aberra Guebrou, C. Symonds, E. Homeyer, J. C. Plenet, Y. N. Gartstein, V. M. Agranovich and J. Bellessa, *Phys. Rev. Lett.*, 2012, **108**, 066401.

7 L. Shi, T. K. Hakala, H. T. Rekola, J. P. Martikainen, R. J. Moerland and P. Törmä, *Phys. Rev. Lett.*, 2014, **112**, 153002.

8 S. Klembt, T. H. Harder, O. A. Egorov, K. Winkler, R. Ge, M. A. Bandres, M. Emmerling, L. Worschech, T. C. H. Liew, M. Segev, C. Schneider and S. Höfling, *Nature*, 2018, **562**, 552–556.

9 C. E. Bardyn, T. Karzig, G. Refael and T. C. H. Liew, *Phys. Rev. B: Condens. Matter Mater. Phys.*, 2015, **91**, 161413.

10 T. Karzig, C. E. Bardyn, N. H. Lindner and G. Refael, *Phys. Rev. X*, 2015, **5**, 031001.

11 M. Ramezani, A. Halpin, A. I. Fernández-Domínguez, J. Feist, S. R. K. Rodriguez, F. J. Garcia-Vidal and J. Gómez Rivas, *Optica*, 2017, **4**, 31–37.

12 S. Kéna-Cohen and S. R. Forrest, *Nat. Photonics*, 2010, **4**, 371–375.

13 G. Khitrova, H. M. Gibbs, M. Kira, S. W. Koch and A. Scherer, *Nat. Phys.*, 2006, **2**, 81–90.

14 D. G. Baranov, M. Wersäll, J. Cuadra, T. J. Antosiewicz and T. Shegai, *ACS Photonics*, 2018, **5**, 24–42.

15 H. X. Xu, E. J. Bjerneld, M. Käll and L. Börjesson, *Phys. Rev. Lett.*, 1999, **83**, 4357–4360.

16 H. X. Xu, J. Aizpurua, M. Käll and P. Apell, *Phys. Rev. E: Stat. Phys., Plasmas, Fluids, Relat. Interdiscip. Top.*, 2000, **62**, 4318–4324.

17 R. Chikkaraddy, B. de Nijs, F. Benz, S. J. Barrow, O. A. Scherman, E. Rosta, A. Demetriadou, P. Fox, O. Hess and J. J. Baumberg, *Nature*, 2016, **535**, 127.

18 O. S. Ojambati, R. Chikkaraddy, W. D. Deacon, M. Horton, D. Kos, V. A. Turek, U. F. Keyser and J. J. Baumberg, *Nat. Commun.*, 2019, **10**, 1049.

19 K. Santhosh, O. Bitton, L. Chuntonov and G. Haran, *Nat. Commun.*, 2016, **7**, 11823.

20 H. X. Leng, B. Szychowski, M. C. Daniel and M. Pelton, *Nat. Commun.*, 2018, **9**, 4012.

21 H. Groß, J. M. Hamm, T. Tufarelli, O. Hess and B. Hecht, *Sci. Adv.*, 2018, **4**, eaar4906.

22 K. D. Park, M. A. May, H. X. Leng, J. R. Wang, J. A. Kropp, T. Gougousi, M. Pelton and M. B. Raschke, *Sci. Adv.*, 2019, **5**, eaav5931.

23 D. Zheng, S. P. Zhang, Q. Deng, M. Kang, P. Nordlander and H. X. Xu, *Nano Lett.*, 2017, **17**, 3809–3814.

24 J. X. Wen, H. Wang, W. L. Wang, Z. X. Deng, C. Zhuang, Y. Zhang, F. Liu, J. C. She, J. Chen, H. J. Chen, S. Z. Deng and N. S. Xu, *Nano Lett.*, 2017, **17**, 4689–4697.

25 J. Cuadra, D. G. Baranov, M. Wersäll, R. Verre, T. J. Antosiewicz and T. Shegai, *Nano Lett.*, 2018, **18**, 1777–1785.

26 M. Stührenberg, B. Munkhbat, D. G. Baranov, J. Cuadra, A. B. Yankovich, T. J. Antosiewicz, E. Olsson and T. Shegai, *Nano Lett.*, 2018, **18**, 5938–5945.

27 T. W. Lo, Q. Zhang, M. Qiu, X. Y. Guo, Y. J. Meng, Y. Zhu, J. J. Xiao, W. Jin, C. W. Leung and D. Y. Lei, *ACS Photonics*, 2019, **6**, 411–421.

28 K. F. Mak and J. Shan, *Nat. Photonics*, 2016, **10**, 216.

29 D. Xiao, G. B. Liu, W. X. Feng, X. D. Xu and W. Yao, *Phys. Rev. Lett.*, 2012, **108**, 196802.

30 A. K. Geim and I. V. Grigorieva, *Nature*, 2013, **499**, 419.

31 F. Xia, H. Wang, D. Xiao, M. Dubey and A. Ramasubramaniam, *Nat. Photonics*, 2014, **8**, 899.

32 X. Z. Liu, T. Galfsky, Z. Sun, F. N. Xia, E. C. Lin, Y. H. Lee, S. Kéna-Cohen and V. M. Menon, *Nat. Photonics*, 2014, **9**, 30.

33 Y. J. Chen, J. D. Cain, T. K. Stanev, V. P. Dravid and N. P. Stern, *Nat. Photonics*, 2017, **11**, 431.

34 S. Dufferwiel, T. P. Lyons, D. D. Solnyshkov, A. A. P. Trichet, F. Withers, S. Schwarz, G. Malpuech, J. M. Smith,

K. S. Novoselov, M. S. Skolnick, D. N. Krizhanovskii and A. I. Tartakovskii, *Nat. Photonics*, 2017, **11**, 497.

35 Z. Sun, J. Gu, A. Ghazaryan, Z. Shotan, C. R. Considine, M. Dollar, B. Chakraborty, X. Z. Liu, P. Ghaemi, S. Kéna-Cohen and V. M. Menon, *Nat. Photonics*, 2017, **11**, 491.

36 S. J. Wang, S. L. Li, T. Chervy, A. Shalabney, S. Azzini, E. Orgiu, J. A. Hutchison, C. Genet, P. Samorì and T. W. Ebbesen, *Nano Lett.*, 2016, **16**, 4368–4374.

37 B. Lee, J. Park, G. H. Han, H. S. Ee, C. H. Naylor, W. J. Liu, A. T. C. Johnson and R. Agarwal, *Nano Lett.*, 2015, **15**, 3646–3653.

38 W. J. Liu, B. Lee, C. H. Naylor, H. S. Ee, J. Park, A. T. C. Johnson and R. Agarwal, *Nano Lett.*, 2016, **16**, 1262–1269.

39 S. J. Wang, Q. Le-Van, F. Vaianella, B. Maes, S. Eizagirre Barker, R. H. Godiksen, A. G. Curto and J. Gomez Rivas, *ACS Photonics*, 2019, **6**, 286–293.

40 B. W. Li, S. Zu, Z. P. Zhang, L. H. Zheng, Q. Jiang, B. W. Du, Y. Luo, Y. J. Gong, Y. F. Zhang, F. Lin, B. Shen, X. Zhu, P. M. Ajayan and Z. Y. Fang, *Opto-Electron. Adv.*, 2019, **2**, 190008.

41 A. Bisht, J. Cuadra, M. Wersäll, A. Canales, T. J. Antosiewicz and T. Shegai, *Nano Lett.*, 2019, **19**, 189–196.

42 H. L. Hu, H. G. Duan, J. K. W. Yang and Z. X. Shen, *ACS Nano*, 2012, **6**, 10147–10155.

43 Y. Q. Chen, Z. Q. Li, Q. Xiang, Y. S. Wang, Z. Q. Zhang and H. G. Duan, *Nanotechnology*, 2015, **26**, 405301.

44 M. W. Knight, J. Fan, F. Capasso and N. J. Halas, *Opt. Express*, 2010, **18**, 2579–2587.

45 A. F. Koenderink, *Opt. Lett.*, 2010, **35**, 4208–4210.

46 A. E. Schlather, N. Large, A. S. Urban, P. Nordlander and N. J. Halas, *Nano Lett.*, 2013, **13**, 3281–3286.

47 M. Kaniber, K. Schraml, A. Regler, J. Bartl, G. Glashagen, F. Flassig, J. Wierzbowski and J. J. Finley, *Sci. Rep.*, 2016, **6**, 23203.

48 J. Merlein, M. Kahl, A. Zuschlag, A. Sell, A. Halm, J. Boneberg, P. Leiderer, A. Leitenstorfer and R. Bratschitsch, *Nat. Photonics*, 2008, **2**, 230.

49 Z. J. Yang, T. J. Antosiewicz and T. Shegai, *Opt. Express*, 2016, **24**, 20373–20381.

50 H. Deng, H. Haug and Y. Yamamoto, *Rev. Mod. Phys.*, 2010, **82**, 1489–1537.

51 T. Devkota, B. S. Brown, G. Beane, K. Yu and G. V. Hartland, *J. Chem. Phys.*, 2019, **151**, 080901.

52 C. Sönnichsen, T. Franzl, T. Wilk, G. von Plessen, J. Feldmann, O. Wilson and P. Mulvaney, *Phys. Rev. Lett.*, 2002, **88**, 077402.

53 P. B. Johnson and R. W. Christy, *Phys. Rev. B: Solid State*, 1972, **6**, 4370–4379.

54 M. A. Green, *Sol. Energy Mater. Sol. Cells*, 2008, **92**, 1305–1310.

55 Y. L. Li, A. Chernikov, X. Zhang, A. Rigosi, H. M. Hill, A. M. van der Zande, D. A. Chenet, E. M. Shih, J. Hone and T. F. Heinz, *Phys. Rev. B: Condens. Matter Mater. Phys.*, 2014, **90**, 205422.

56 A. Thilagam, *J. Appl. Phys.*, 2014, **116**, 053523.

57 J. W. Sun, H. T. Hu, D. Zheng, D. X. Zhang, Q. Deng, S. P. Zhang and H. X. Xu, *ACS Nano*, 2018, **12**, 10393–10402.

58 R. Verre, D. G. Baranov, B. Munkhbat, J. Cuadra, M. Käll and T. Shegai, *Nat. Nanotechnol.*, 2019, **14**, 679–683.